HHS Public Access

Author manuscript

Cell Rep. Author manuscript; available in PMC 2019 March 20.

Published in final edited form as:

Cell Rep. 2019 March 05; 26(10): 2540–2548.e4. doi:10.1016/j.celrep.2019.01.112.

The F-BAR Domain of Rga7 Relies on a Cooperative Mechanism of Membrane Binding with a Partner Protein during Fission Yeast Cytokinesis

Yajun Liu[1,4], **Nathan A. McDonald**[3,4,5], **Shelby M. Naegele**[1], **Kathleen L. Gould**[3,*], and **Jian-Qiu Wu**[1,2,6,*]

[1]Department of Molecular Genetics, The Ohio State University, Columbus, OH 43210, USA

[2]Department of Biological Chemistry and Pharmacology, The Ohio State University, Columbus, OH 43210, USA

[3]Department of Cell and Developmental Biology, Vanderbilt University, Nashville, TN 37240, USA

[4]These authors contributed equally

[5]Present address: Department of Biology, Stanford University, Stanford, CA 94305, USA

[6]Lead Contact

SUMMARY

F-BAR proteins bind the plasma membrane (PM) to scaffold and organize the actin cytoskeleton. To understand how F-BAR proteins achieve their PM association, we studied the localization of a *Schizosaccharomyces pombe* F-BAR protein Rga7, which requires the coiled-coil protein Rng10 for targeting to the division site during cytokinesis. We find that the Rga7 F-BAR domain directly binds a motif in Rng10 simultaneously with the PM, and that an adjacent Rng10 motif independently binds the PM. Together, these multivalent interactions significantly enhance Rga7 F-BAR avidity for membranes at physiological protein concentrations, ensuring the division site localization of Rga7. Moreover, the requirement for the F-BAR domain in Rga7 localization and function in cytokinesis is bypassed by tethering an Rga7 construct lacking its F-BAR to Rng10, indicating that at least some F-BAR domains are necessary but not sufficient for PM targeting and are stably localized to specific cortical positions through adaptor proteins.

In Brief

Liu et al. show that the Rga7 F-BAR domain binds an adaptor protein Rng10, which contains a second membrane-binding module, to enhance Rga7 membrane avidity and stabilize its membrane

*Correspondence: kathy.gould@vanderbilt.edu (K.L.G.), wu.620@osu.edu (J.-Q.W.).

AUTHOR CONTRIBUTIONS

Y.L., N.A.M., K.L.G., and J.-Q.W. designed the experiments. Y.L., N.A.M., and S.M.N. performed the experiments and analyzed the data. Y.L., N.A.M., K.L.G., and J.-Q.W. wrote the manuscript.

DECLARATION OF INTERESTS

The authors declare no competing interests.

SUPPLEMENTAL INFORMATION

Supplemental Information can be found with this article online at https://doi.org/10.1016/j.celrep.2019.01.112.

association. The authors reveal a mechanism by which F-BAR domains can achieve high-avidity binding with the plasma membrane.

Graphical Abstract

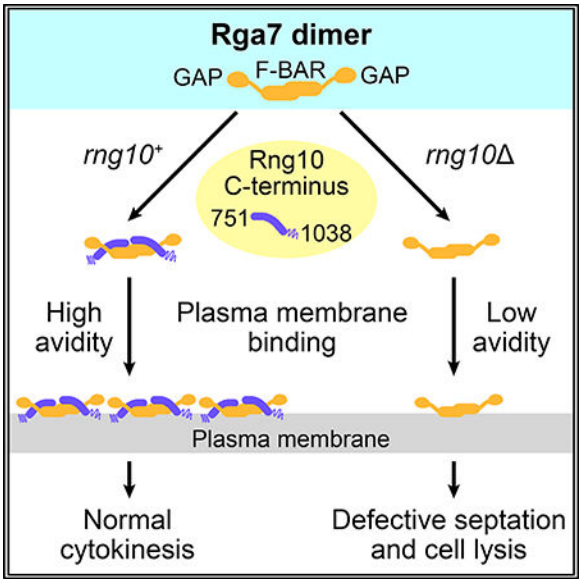

INTRODUCTION

The F-BAR (Fer/CIP4 homology-Bin-Amphiphysin-Rvs)-domain superfamily broadly functions to link the plasma membrane (PM) to the actin cytoskeleton (Liu et al., 2015; Roberts-Galbraith and Gould, 2010; Salzer et al., 2017). As such, F-BAR proteins play major roles in membrane trafficking, cell morphology, cell motility, and cell division.

Membrane binding is an intrinsic property of all F-BAR domains (Begonja et al., 2015; Frost et al., 2009; Itoh and Takenawa, 2009; Liu et al., 2015; Takeda et al., 2013). These domains homodimerize to form crescent-shaped or flat modules that interact with anionic membranes with modest affinity (Almeida-Souza et al., 2018; Kelley et al., 2015a; Lefèbvre et al., 2012; Moravcevic et al., 2015; Soulard et al., 2002). F-BAR domains can achieve stronger avidity for membranes by homo-oligomerizing through tip-to-tip or tip-to-core interactions (Frost et al., 2009; McDonald et al., 2015; Shimada et al., 2007). The majority of F-BAR proteins contain only F-BAR domains for membrane binding, with the exception of Fes and Fer, which have an adjacent FX domain as a second membrane-binding module (Itoh et al., 2009). Although interaction networks established through other domains such as SH3, μHD, RhoGAP (guanosine triphosphatase [GTPase]-activating protein), tyrosine kinase, and C1 can influence discrete localizations (Aspenström, 2009; Salzer et al., 2017; Roberts-Galbraith and Gould, 2010), in general, F-BAR proteins are thought to depend on the lipid binding of F-BAR domains for membrane association and proper intracellular targeting (Frost et al., 2009; McDonald and Gould, 2016b; Mim and Unger, 2012; Qualmann et al., 2011; Salzer et al., 2017). How F-BAR domains could mediate subcellular targeting is not clear, although several hypotheses have been suggested. One possibility is that F-BARs

bind certain lipid head groups preferentially (e.g., phosphoinositides [PIPs]). However, few F-BAR domains contain specific PIP-binding pockets, and most are able to bind membranes with a wide range of compositions *in vitro* (Frost et al., 2009; Itoh and Takenawa, 2009; McDonald and Gould, 2016b). Another proposed localization mechanism is sensing subcellular membrane curvature (Mim and Unger, 2012). This hypothesis has seemed most relevant for F-BAR proteins involved in endocytosis, in which highly curved membrane intermediates are formed, and different F-BARs assemble on the budding vesicle in a defined order (Taylor et al., 2011). However, the localization timings do not correlate with the curvature of the F-BAR crescent (Qualmann et al., 2011), and *in vitro*, these F-BAR domains bind to liposomes with varied membrane curvatures (Itoh et al., 2005; McDonald and Gould, 2016b). Thus, it remains unclear mechanistically how most F-BAR proteins target to the correct subcellular localization.

The *Schizosaccharomyces pombe* F-BAR protein Rga7 localizes to the division site and functions during late cytokinesis; rga7 mutants lyse at cell separation due to defective septa (Arasada and Pollard, 2015; Liu et al., 2016; Martín-García et al., 2014). While Rga7 function in cytokinesis requires its proline-rich middle region and a C-terminal RhoGAP domain in addition to its F-BAR domain, Rga7 localization requires its F-BAR domain and a binding partner, Rng10 (Arasada and Pollard, 2015; Liu et al., 2016).

Here, we report the molecular mechanism by which Rng10 cooperates with the Rga7 F-BAR domain to localize Rga7 to the PM of the division site. We find that the Rga7 F-BAR domain, which binds phospholipids similarly to other F-BAR domains, also binds a motif within the Rng10 C terminus. An adjacent Rng10 motif provides a second membrane-binding module. The Rng10-Rga7 complex has high membrane avidity, and complex formation is required for efficient division site localization. This targeting mechanism provides an example in which an F-BAR domain binds the PM and a partner protein simultaneously and suggests a novel mechanism by which F-BAR domains are recruited by coincident phospholipid and protein binding. As the majority of the BAR superfamily proteins contain only the F-BAR/BAR domains as a membrane-binding module (Liu et al., 2015; McDonald and Gould, 2016b; Salzer et al., 2017), our findings reveal a missing mechanism whereby this low-affinity module can achieve high-avidity binding with the PM and will inspire a search for F-BAR/BAR domain adaptors in other organisms.

RESULTS AND DISCUSSION

The Rng10 C Terminus Is Required for Division-Site Localization of the F-BAR Protein Rga7

Rga7 localization and function during septation requires the coiled-coil protein Rng10 (Figure 1A; Liu et al., 2016). We defined the regions of Rng10 required for Rga7 localization. Rga7 localized to the division site and cell tips in all Rng10 N-terminal truncations tested (Figures 1B and S1A), but failed to localize in Rng10 C-terminal truncations (Figures 1B and S1B). Since Rga7 required minimally Rng10(751–1,038) for colocalization to the pre-constriction ring, constricting ring, and a disk lining the septum at the division site (Figures 1B and S1C), we concluded that the Rng10 C terminus is sufficient to localize Rga7.

To confirm that the Rng10 C terminus is sufficient for Rga7 subcellular localization, we tested whether artificially mitochondria-localized Rng10(751–1,038) could recruit Rga7. The mitochondrial outer membrane protein Tom20 was tagged with GFP-binding protein (GBP) (Rothbauer et al., 2008; Yamamoto et al., 2011) in combination with monomeric EGFP (mEGFP)/mECitrine-tagged Rng10 constructs. The Rng10 constructs were robustly recruited to the mitochondria by Tom20-GBP, while tdTomato, mScarlet-I, or mCherry tagged Rga7 were not (Figure S1D). As predicted, Rng10 and Rng10(751–1,038), but not Rng10(1–750), recruited Rga7 to mitochondria (Figure S1E). These data indicate that the Rng10 C terminus (amino acids [aa] 751–1,038) is sufficient to direct Rga7 to the division site.

The Rng10 C Terminus Directly Interacts with the Rga7 F-BAR Domain to Regulate Rga7 Localization

Because the Rga7 F-BAR domain (aa 1–320) is sufficient for Rga7 localization (Arasada and Pollard, 2015), we hypothesized that the F-BAR domain interacts with the Rng10 C terminus. Rng10(751–1,038) localized not only full-length Rga7 but also the F-BAR domain alone (Figure 1C). To test for a direct interaction, we performed *in vitro* binding assays using recombinant Rng10 C terminus and the Rga7 F-BAR (Figures 1D and S2A). GST-Rng10(751–1,038) efficiently bound His_6-Rga7(1–320) with a dissociation constant (K_d) of 0.43 μM (Figures 1D, 1E, and S2B). F-BAR domains are typically obligate dimers that can oligomerize to form higher-order assemblies (McDonald and Gould, 2016b). The Rga7 F-BAR is also a dimer, and the binding to Rng10(751–1,038) does not appreciably affect Rga7 F-BAR oligomeric states (Figure S2C). Defining the Rga7-binding motif within Rng10 further, we found that Rng10(751–950) bound Rga7(1–320) with a similar K_d of 0.69 μM (Figures 1F, 1G, and S2B), and Rng10(751–950) could mistarget Rga7 to mitochondria (Figures 1H and S1D). We conclude that Rng10(751–950) interacts directly with the Rga7 F-BAR domain. The Rga7 F-BAR domain thus joins a growing list of F-BAR domains reported to bind directly to a second protein; other examples include the F-BARs of *S. pombe* Cdc15, *Saccharomyces cerevisiae* Hof1, mammalian Pacsin2, and human proline-serine-threonine phosphatase-interacting protein (PSTPIP) (Hansen et al., 2011; Senju et al., 2011; Begonja et al., 2015; Shoham et al., 2003; Willet et al., 2015; Garabedian et al., 2018). However, none of these previously reported interactions are known to influence F-BAR protein targeting, and therefore Rga7 emerges as an example in which binding of the F-BAR domain to a second protein regulates F-BAR protein localization.

The Rng10 C Terminus Also Contains a Membrane-Binding Motif

Although the tail of Rng10 C terminus (aa 951–1,038) is dispensable for the Rng10-Rga7 interaction *in vitro* (Figures 1F and S2D), it is crucial for Rga7 localization *in vivo* (Figure 2A). Rga7 levels at the pre-constriction ring, the constricting ring, and as a disk lining the septum were similar to wild-type (WT) in *rng10(751–1,038)* cells but reduced significantly in *rng10(751–950)* and in *rng10(951–1,038)* and *rng10(1–750)* cells that lack the Rng10-Rga7 binding interface (Figure 2A). The low division site levels in some Rng10 mutants were not due to a decrease in cellular Rga7 protein concentration (Figure S2E). We therefore hypothesized that Rng10(951–1,038) contains an additional protein or membrane-binding motif that modulates the division site targeting of Rga7. Rng10(951–1,038), but not

Rng10(751–950), bound liposomes *in vitro* (Figure 2B), but with no apparent lipid specificity beyond a general one for negatively charged PIP species (Figure 2C). A sequence analysis of Rng10(951–1,038) revealed no predicted secondary structure or identifiable membrane-binding motif, but it contains 20% positively charged residues and has an isoelectric point (pI) of 10.4, which is consistent with an electrostatic interaction with anionic membranes. Circular dichroism (CD) revealed that Rng10(951–1,038) adopts a random coil (unfolded) conformation evidenced by its strong downward peak at 200 nm (Figure 2D). Thus, Rng10(951–1,038) is unstructured but capable of binding membranes. In accord Rng10(951–1,038) decorated the entire PM independent of Rga7 (Figure 2E).

Mechanism of Rga7 F-BAR Membrane Binding

That Rng10 contains a membrane-binding motif linked to an Rga7 interaction motif raised the question of whether membrane binding by the Rga7 F-BAR is at all important for Rga7 localization and function. To determine whether and how the Rga7 F-BAR binds membranes, we generated a structural model of the Rga7 F-BAR dimer (Figure 3A) based on the closely related *S. cerevisiae* Rgd1 F-BAR that has been crystallized (Moravcevic et al., 2015). The model predicted the conservation of a PIP_2 binding pocket near the kinks in the F-BAR arms (blue residues, Figure 3A). Additional positively charged residues were identified on the concave face of the Rga7 F-BAR that could contribute to membrane binding (orange and red residues, Figure 3A). We mutated patches of these basic residues and tested the mutants' ability to bind membranes *in vitro*. While WT Rga7 F-BAR bound strongly to liposomes, mutation of the PIP_2 pocket decreased its affinity (Figures 3B and 3C). Combining mutations in the PIP_2 pocket and in positively charged patches along the core of the domain and at its tips abolished membrane binding (Figures 3B and 3C). These mutations also prevented the Rga7 F-BAR from binding and tubulating giant unilamellar vesicles (GUVs) (Figure S3A), but they did not prevent binding to the Rng10 C terminus *in vitro* (Figures S2F and S2G), suggesting that the membrane- and Rng10-binding sites are on opposite faces of the Rga7 F-BAR domain. When expressed in COS-7 cells, the Rga7 F-BAR WT, but not membrane-binding mutants, induced tubules that also contained the Rng10 C terminus (Figures S3B and S3C).

We next tested whether Rga7 preferentially bound membranes of a specific lipid composition. As predicted by the presence of a PIP_2 binding pocket, the Rga7 F-BAR preferred membranes rich in PI(4)P and PI(4,5)P_2 (Figure 3D). The PIP_2 pocket mutant lost this specificity, binding membranes rich in phosphatidic acid (PA) equally well (Figure 3D).

To determine whether F-BAR membrane binding is required for Rga7 localization when Rng10 is present, we integrated the F-BAR lipid-binding mutants into *rga7*Δ cells under the endogenous *rga7* promoter. The PIP_2 pocket mutant still localized to the division site, but with a lower level than WT (Figure 3E), consistent with its membrane-binding properties *in vitro* (Figure 3B). However, combining the PIP_2 binding mutations with core and tip patch mutations eliminated the localization of the Rga7 F-BAR to the division site (Figure 3E). Although the membrane-binding mutants were present at lower levels than WT Rga7 (Figure 3F), sufficient protein was produced for the detection of medial localization if it had occurred and overexpression of the mutants did not restore membrane localization (Figure

S3D). We conclude that the Rga7 F-BAR interacts with membranes in a canonical fashion, and its membrane-binding ability is required but insufficient for Rga7 localization.

The Rng10-Rga7 Complex Enhances Rga7 Membrane Binding and Function at Physiological Concentrations

Since Rng10 and Rga7 directly interact and both bind membranes, we next asked whether the complex had different membrane-binding properties than the individual proteins. Rga7 F-BAR binding to liposomes was increased when Rng10(751–1,038) was present compared to the F-BAR alone (Figure 4A). When Rng10 lacked either the Rga7- or membrane-binding motif, this increase was abolished. The increase was particularly pronounced at the lower protein concentrations (Figure 4A, inset) that match the global concentrations of Rng10 and Rga7 in cells at 0.38 and 1.00 μM, respectively (Figure 4B; see Method Details). The Rga7 level at the division site was only ~1.3×higher than Rng10, suggesting a 1:1 stoichiometry for Rng10 and Rga7 on the PM (Figure 4C). Thus, our results suggest that Rga7 F-BAR and Rng10(751–1,038) bind cooperatively to the PM for division-site localization.

To evaluate how the Rng10-Rga7 interaction affects cell division, we quantified cell lysis, indicative of septation failure (Liu et al., 2016), in the Rng10 and Rga7 mutants described above. The *rga7*Δ and *rng10*Δ mutants had mild lysis at 25°C and severe lysis at 36°C, as did Rng10 mutants lacking Rga7 and/or membrane-binding motifs. In contrast, Rng10(751–1,038) had low levels of lysis (Figure 4D). Thus, Rng10 interactions with both Rga7 and the PM are critical for Rga7 function.

Although the Rga7 F-BAR alone localizes to the division site in *rng10*$^{+}$ cells (Figure 3E; Arasada and Pollard, 2015), >40% rga7(1–320) cells lysed at 36C, comparable to the ~50% lysis of *rga7*Δ cells (Figure 4D), indicating that the Rga7 central region and/or GAP domain contribute to Rga7 function (Figure 1A). This result was unexpected because Rga7 GAP catalytic activity was reported to be dispensable for Rga7 function (Martín-García et al., 2014). We therefore tested whether localizing the Rga7 central and GAP domains to the PM is the critical function of its F-BAR domain by artificially recruiting them to the division site with Rng10-GBP. GFP-Rga7(277–695) alone, lacking the majority of the F-BAR domain, could not localize to the PM, resulting in massive cell lysis (58%) similar to *rga7*Δ (Figures 4E and S3E; Martín-García et al., 2014). However, Rng10-GBP restored GFP-Rga7(277–695) localization to the division site and significantly reduced cell lysis (Figures 4E and S3E). Thus, targeting Rga7 central and GAP domains to the PM, but not other possible activities such as membrane tubulation (Figures S3A and S3B) or curvature sensing, is the critical function of Rga7 F-BAR.

Our data indicate that the interaction between the Rga7 F-BAR and Rng10 ensures the division site localization of Rga7 by elevating its membrane-binding avidity, and this supports efficient septation during cytokinesis. Analogous examples of such cooperativity between intramolecular dual membrane-binding domains exist in a few F-BAR and N-BAR proteins (Carman and Dominguez, 2018). The Fes F-BAR domain and adjacent FX domain cooperate to increase membrane avidity (Itoh et al., 2009). APPL1 contains an N-BAR domain and an immediately adjacent pleckstrin homology domain, which also binds phospholipids (Lemmon, 2004). The sorting nexin Snx9 contains a phox homology domain

that binds phosphatidylinositols preceding the N-BAR domain (Pylypenko et al., 2007). The Rga7 F-BAR appears to use a similar strategy of a second membrane-binding domain, but in this case, within its partner, Rng10. In general, individual F-BARs are relatively weak membrane-binding domains; it is only by interacting with another membrane-binding domain or by extensive oligomerization as seen in many other F-BARs (McDonald and Gould, 2016b) that a stable interaction with the membrane can be established.

Furthermore, we have mechanistically illustrated a case in which the ability of an F-BAR domain to bind membranes is necessary but not sufficient for cellular localization. Instead, the domain relies on linkage to an adaptor protein that has additional membrane-binding potential to cooperatively achieve stable and specific membrane associations (Figure 4F). This strategy of membrane localization could be particularly useful for exerting spatial and temporal control of dynamic F-BAR localization since interactions between different adapters can be regulated. Because the majority of the BAR superfamily proteins contains only the F-BAR/BAR domains as a low-affinity membrane-binding module (Liu et al., 2015; McDonald and Gould, 2016b; Salzer et al., 2017), we expect that additional examples of protein adapters that modulate F-BAR/ BAR protein localization and function will be identified in the future.

STAR★METHODS

CONTACT FOR REAGENT AND RESOURCE SHARING

Further information and requests for resources and reagent should be directed to and will be fulfilled by the Lead Contact, Jian-Qiu Wu (wu.620@osu.edu).

EXPERIMENTAL MODEL AND SUBJECT DETAILS

Fission Yeast—Table S1 lists the *S. pombe* strains used in this study. Cells were grown exponentially in YE5S or EMM5S liquid media for 1~2 days. Detailed growth conditions see individual experiments in Method Details.

Escherichia coli—*E. coli* strain BL21(DE3)pLysS (694513; Novagen, EMD Chemicals, Darmstdt, Germany) were grown in LB media at 37°C and induced with 1 mM isopropyl-β-D-thiogalactoside (IPTG) for 2–4 h at 30 or 37°C.

Cell Line—COS-7 cells were cultured in DMEM media containing 10% fetal bovine serum (FBS), and transfected with a Lipofectamine 2000 reagent according to the manufacturer's protocols.

METHOD DETAILS

Molecular Biology Methods—Full length and truncated genes were tagged C-terminally at their native chromosomal loci and expressed under their endogenous promoters by PCR-based gene targeting (Bähler et al., 1998). N-terminal truncations and tagging of *rng10* were constructed with pFA6a-kanMX6-Prng10-mECitrine (JQW908) as the PCR template, resulting in strains under the control of the native promoter of *rng10* (−510 to +6 bp). N-terminal tagging of Rga7 F-BAR mutants was constructed using pFA6a-kanMX6-P3nmt1-

mECitrine (JQW331). All strains from gene targeting were confirmed by PCR and visual screening if possible. To minimize cell lysis, some spores from crosses were germinated on medium with 1.2 M sorbitol.

Rga7 F-BAR lipid-binding mutants were synthesized in a pET-15b protein expression plasmid by GenScript (Piscataway, NJ). The resulting plasmids (JQW923-JQW925) were used as templates for PCR and further cloning. The mutants are: PIP_2 mutant, R144D/K148E; PIP_2 + Core mutant, K60E/K67E/K78E/K82E/R144D/K148E; PIP_2 + Core + Tips mutant, K60E/K67E/K78E/K82E/R144D/K148E/K167E/R181D/K194E. To integrate these mutations into the *rga7* locus, the whole *rga7* ORF was deleted using pFA6a-*ura4*$^+$ (JQW328) to obtain the *rga7*Δ::*ura4*$^+$ strain. Then *rga7*(1–320) sequences with the desired mutations were amplified from plasmids JQW923-JQW925 using primers containing sequences of the 5′ and 3′ UTRs of *rga7*. The PCR products were transformed into the *rga7*Δ::*ura4*$^+$ cells. Positive transformants were selected by resistance to 5-fluoroorotic acid (5-FOA) and confirmed by sequencing.

To construct protein expression plasmids, *rng10* and *rga7* fragments were amplified from genomic DNA. Rng10 fragments were cloned into pQE-80L (His tag) at SacI and PstI sites, or pGEX-4T-1 (GST tag) at EcoRI and NotI sites. Rga7(1–320) was cloned into pQE-80L at BamHI and SalI sites. Synthesized Rga7 F-BAR lipid-binding mutant DNAs were amplified and re-cloned into pEGFP-C1 at EcoRI and BamHI sites and pET15b-GFP at NdeI and BamHI sites.

Microscopy—Confocal microscopy was performed as previously described (Liu et al., 2016). For analyses of cell lysis, cells were first grown exponentially in YE5S liquid medium at 25°C for ~40 h and then imaged or shifted to 36°C for 4 h before imaging. Cells were collected by centrifugation at 3000 rpm for 30 s and imaged on the glass slide with a pad of YE5S with 20% gelatin and 50 nM *n*-propyl-gallate (*n*-PG) at room temperature. For fluorescence microscopy, cells were grown exponentially in YE5S liquid medium at 25°C for 2 days, or in EMM5S liquid medium at 25°C for 24 h to induce overexpression of Rga7 F-BAR mutants. Cells were centrifuged at 3000 rpm for 30 s and then washed twice with EMM5S to reduce autofluorescence. *n*-PG from a 10 × stock made in EMM5S were added to EMM5S in the second wash to a final concentration of 50 nM, to reduce phototoxicity and photobleaching (Giloh and Sedat, 1982; Laporte et al., 2011). Live cells were imaged on a glass slide with a pad of EMM5S with 20% gelatin (Sigma-Aldrich, St. Loius, MO) and 50 nM *n*-PG at 23–24°C.

Fission yeast cells were imaged on two microscopy systems with 100x/1.4 numerical aperture (NA) Plan-Apo objective lenses (Nikon, Melville, NY). Differential interference contrast (DIC) images for quantification of cell lysis were taken using a Nikon Eclipse Ti inverted microscope equipped with a Nikon DS-QI1 cooled digital camera. Fluorescence images were taken using a spinningdisk confocal system (UltraVIEW Vox CSUX1 system; PerkinElmer, Waltham, MA) with 440-, 488-, 515-, and 561-nm solid-state lasers and back thinned electron-multiplying charge-coupled device (EMCCD) cameras (C9100–13 or C9100–23B; Hamamatsu Photonics, Bridgewater, NJ) on a Nikon Ti-E microscope. COS-7 cells and giant unilamellar vesicles were imaged on a Personal Deltavision system (GE)

equipped with 63X 1.4NA objective, Coolsnap2 CCD camera, and 488-, 561-, and 647-nm lasers.

Image Analysis—Images were processed and analyzed using Volocity (PerkinElmer) and ImageJ (National Institutes of Health, Bethesda, MD). Fluorescence images in figures are maximum-intensity projections with z sections spaced at 0.5 μm except where noted. Some images contain lysed cells, which have bright autofluorescence.

Protein Purification and *in vitro* Binding Assay—Purifications of His_6- or GST-tagged proteins from *E. coli* were carried out as previously described (Zhu et al., 2013). His_6-tagged proteins were purified with Talon metal affinity resin (635501; Clontech, Mountain View, CA) in extraction buffer (50 mM sodium phosphate, pH 8.0, 500 mM NaCl, 10 mM β-mercaptoethanol, 1 mM PMSF, and 10 mM imidazole) with EDTA-free protease inhibitor tablet (Roche) and eluted with elution buffer (50 mM sodium phosphate, pH 8.0, 500 mM NaCl, 10 mM β-mercaptoethanol, 1 mM PMSF, and 200 mM imidazole). GST-tagged proteins were purified with Glutathione-Sepharose beads (17–5132-01; GE Healthcare) in phosphate extraction buffer (50 mM sodium phosphate, pH 6.0, 200 mM NaCl, 1 mM PMSF, and 1 mM DTT) with EDTA-free protease inhibitor tablet and eluted with glutathione (50 mM sodium phosphate, pH 6.1, 200 mM NaCl, 1 mM PMSF, 1 mM DTT, 100 μM glutathione). The purified proteins were then dialyzed into the final reaction buffer.

For *in vitro* binding assay between GST-Rng10(751–1038) and His_6-Rga7(1–320), purified proteins were dialyzed into the binding buffer (100 mM NaCl, 20 mM imidazole, 1 mM DTT, pH 7.0). GST-Rng10(751–1038) or GST control (Zhu et al., 2013) was incubated with glutathione-Sepharose beads for 2 h at 4°C and washed 4 times with the binding buffer to remove unbound proteins. His_6-Rga7(1–320) or His_6-mEGFP control (Wu and Pollard, 2005) was then incubated with the beads for 2 h at 4°C. After 5 washes with the binding buffer, the beads were boiled with sample buffer for 5 min. Then the samples were run on SDS-PAGE gel and detected with Coomassie Blue staining.

For *in vitro* binding assays between GST-Rng10(751–950/1038) and His_6-Rga7(1–320) mutants, GST-Rng10(751–950/1038) was first purified and dialyzed into the binding buffer (50 mM sodium phosphate, pH 7, 200 mM NaCl, 1 mM PMSF, and 1 mM DTT) and then incubated with glutathione-Sepharose beads for 1 h at 4°C. The beads were washed once, resuspended, and aliquoted in equal volume. His_6-Rga7(1–320) wild-type control and mutants were prepared in small scale by resuspending cells in the binding buffer and sonicating to break the cells. Cell lysates were centrifuged at 15,000 rpm for 15 min at 4°C. Rga7 proteins in the supernatant were normalized to similar protein levels and added to the aliquoted GST-Rng10 bound beads. After 1 h incubation at 4°C, beads were washed 3 times with the binding buffer, and boiled with sample buffer. Then the samples were run on SDS-PAGE gel and detected with western blotting.

For measuring the K_d between Rng10(751–950/1038) and Rga7(1–320), we followed the described methods and guidelines (Lee et al., 1999; Pollard, 2010). The procedure was similar to the *in vitro* binding assays described in the previous paragraph except different

concentrations of beads and purified GST-Rng10(751–950/1038) were incubated with the same concentration of His_6-Rga7(1–320) from large-scale purification. Total amount of bead bound GST-Rng10(751–950/1038) was estimated by subtracting the remaining proteins in the supernatant (including proteins released during washing) from the total input. We formed a GST-Rng10(751–950/1038) concentration gradient by adding different volumes of GST-Rng10(751–950/1038) bound beads (0, 20, 50, 80, 100, 150, 200, 250, 300, 350, and 400 μl) to each tube. The same volumes of GST bound beads were used as the control. Binding buffer and a final concentration of 1 μM His_6-Rga7(1–320) were added to a final volume of 500 μl for each tube. After incubation for 10 min at 4°C, the beads were spun down at 15,000 rpm for 5 min, supernatant samples removed from the reactions were boiled with sample buffer, run on an SDS-PAGE gel, and detected with Coomassie Blue staining.

Liposome Co-pelleting Assays—Liposomes were prepared as previously described (McDonald et al., 2015). Lipid chloroform stocks (Avanti Polar Lipids, Alabaster, AL) were mixed at the desired ratios, vacuum dried into a thin film in a glass tube, and resuspended at 1 mg/ml in 20 mM Tris, pH 8.0, 150 mM NaCl buffer with vortexing. The resulting liposome mix was freeze-thawed 10x and passed through an 800 nm liposome extruder (Avanti Polar Lipids, Alabaster, AL). 100 μl liposomes were mixed with 100 μl purified Rga7 or Rng10 protein at the indicated concentrations (or 20 μg when not indicated) and incubated for 15 min at room temperature. Bound liposomes were centrifuged at 150,000 g for 15 min and supernatant (unbound) and pellet (bound) fractions were separated and run on an SDS-PAGE for Coomassie blue detection.

Giant unilamellar vesicles were formed as previously described (McDonald and Gould, 2016a). Chloroform lipid stocks of the desired composition were evaporated on ITO-coated glass coverslides. Coverslides were assembled into a 1 mm thick chamber filled with a 20 mM HEPES, pH 7.4, 500 mM sucrose solution. A 10 Hz, 2.5 V sine current was passed across the chamber for 2 h to electroform the GUVs.

Circular Dichroism and Structural Modeling—The CD spectrum was collected using Jasco J815 spectropolarimeter (Easton, MD, USA) under UV spectroscopy in 1-cm quartz cuvettes at 25°C. CD scans ranged from 180 to 300 nm at a scan rate of 200 nm/min with 1 s interval. Reactions were performed in 25 mM potassium phosphate, pH 7.0 with a protein concentration of at least 10 μM. Data analyses were carried out using K2D3 algorithm to predict secondary structures (Louis-Jeune et al., 2012). The Rga7 F-BAR structure was modeled using the Phyre2 server (Kelley et al., 2015b) based on the *S. cerevisiae* Rgd1 crystal structure (Moravcevic et al., 2015).

Analytical Ultracentrifugation—Purified His_6-Rga7 F-BAR was diluted to a final concentration of 0.5 mg/ml before ultracentrifugation. Purified GST-Rng10(751–1038) was added at equimolar concentration. A sedimentation experiment was run at 42,000 rpm at 4°C on an Optima XLI ultracentrifuge (Beckman-Coulter) with a four-hole An60Ti rotor containing 1.2 cm path-length sapphire windows. 280 nm scan data were analyzed with SedFit (version 14.81) using 250 scans collected ~2 min apart (Schuck, 2000). Size distributions were determined for a confidence level of p = 0.95 and resolution of n = 200.

Cell Culture—COS-7 cells were transfected with a Lipofectamine 2000 reagent according to the manufacturer's protocols. Membranes were labeled with the CellMask Deep Red reagent (Thermo Fisher). Cells were harvested with trypsin and centrifugation, and lysed in RIPA buffer (25 mM Tris, pH 7.4, 150 mM NaCl, 1% NP-40, 0.5% sodium deoxycholate, 0.1% SDS) before western blotting.

Western Blotting—Rga7 immunoblotting was carried out as previously described (Liu et al., 2016). Lyophilized cells (~5 mg) were ground into a homogeneous powder and mixed with IP buffer (1% NP-40 buffer [50 mM 4-(2-hydroxyethyl)-1-piperazineethanesulfonic acid [HEPES], pH 7.5, 100 mM NaCl, 1 mM EDTA, 1% NP-40, 50 mM NaF, 20 mM glycerophosphate, and 0.1 mM Na_3VO_4], 1 mM PMSF, and protease inhibitor [Roche]). Sample buffer was added to the lysate and boiled. Protein samples were separated on an SDS-PAGE gel and detected with (1) a monoclonal anti-GFP antibody (1:2000 dilution; 11814460001; Roche, Mannheim, Germany) or a TAT1 antibody for tubulin (1:20,000 dilution; (Woods et al., 1989); and (2) a secondary antibody anti-mouse immunoglobulin G (1:5000 dilution; A4416, Sigma-Aldrich). ECL (SuperSignal Maximum Sensitivity Substrate, Thermo Fisher Scientific) was used to develop the protein bands on film (BioMax MR; Kodak, Rochester, NY).

For *in vitro* binding assays between GST-Rng10(751–950/1038) and His_6-Rga7(1–320) wild-type control and three mutants, inputs and bound proteins were detected with monoclonal anti-His (1:20,000 dilution; 631212, Clontech) or anti-GST (1:20,000 dilution; NB600–446, Novus Biologicals) antibodies. Secondary anti-mouse fluorescent antibody (92568070, LI-COR) was used at 1:10,000 dilution. Protein bands were detected using LI-COR (Odyssey CLx) at 700 nm channel.

COS-7 cell lysates were separated on an SDS-PAGE gel and detected with a monoclonal anti-GFP primary antibody (1:1000; Roche) and anti-mouse fluorescent secondary antibody (LI-COR) before detection using a LI-COR Odyssey.

QUANTIFICATION AND STATISTICAL ANALYSIS

Protein molecular numbers were calculated from quantifying fluorescence intensity (Deng et al., 2014; Liu et al., 2016). Only the central ~75% of cells in the imaging field were analyzed to minimize the effects of uneven illumination. We summed intensity from 13 z sections at 0.5 μm spacing. For global protein level quantification, the polygon region of interest (ROI) tool in ImageJ was applied to trace cell boundaries. Then WT cells with no fluorescent tag were used to deduct the background. Some of the intensities were converted to concentrations and molecule numbers using a protein standard curve generated from proteins with known molecule numbers (Liu et al., 2016; Wu and Pollard, 2005). The global concentration was calculated using mean molecules and a cytoplasm volume of 27 μm^3 that occupies ~30% of a total cell volume (Wu and Pollard, 2005)

To quantify protein levels on the PM at the cell side, mean intensity of the PM between the division site and the cell tips was measured at the middle z section. Background was subtracted using cytoplasm mean intensity (avoiding nucleus region).

For measuring the K_d between two proteins, intensity for each Coomassie-stained protein band was measured and background subtracted. We defined the intensity of the sample without beads as 100% and normalized others accordingly, which corresponded to unbound proteins. The percentages of bound His_6-Rga7 (1–320) were calculated as a function of the GST-Rng10(751–950/1038) concentrations. Analyzed data were plotted and fitted in KaleidaGraph (Synergy Software) using the equation $y = B_{max}$ (x/[x + K_d]), where B_{max} is the maximal specific binding.

Data in figures are mean ± SEM except where noted. The *P* values in statistical analysis were calculated using a one-way ANOVA and Tukey's post hoc analysis.

Supplementary Material

Refer to Web version on PubMed Central for supplementary material.

ACKNOWLEDGMENTS

We thank Rebeca Martín-García, Pilar Pérez, and Thomas Pollard for strains; Christine Wachnowsky from the James Cowan lab and Eunjeong Lee from the Zhengrong (Justin) Wu lab for technical support; and the Anita Hopper, Dmitri Kudryashov, James Hopper, and Stephen Osmani laboratories for equipment. We are grateful to Janel Beckley, Sierra Cullati, MariaSanta Mangione, Chloe Snider, and Alaina Willet from the Gould lab and members of the Wu lab for helpful comments on the manuscript. This work was supported by a Pelotonia Graduate Fellowship (to Y.L.), an American Heart Association fellowship (15PRE21780003 to N.A.M.), and grants from the National Institute of General Medical Sciences of the NIH (GM101035 to K.L.G. and GM118746 to J.Q.W.).

REFERENCES

Almeida-Souza L, Frank RAW, García-Nafría J, Colussi A, Gunawardana N, Johnson CM, Yu M, Howard G, Andrews B, Vallis Y, and McMahon HT (2018). A flat BAR protein promotes actin polymerization at the base of clathrin-coated pits. Cell 174, 325–337. [PubMed: 29887380]

Arasada R, and Pollard TD (2015). A role for F-BAR protein Rga7p during cytokinesis in *S. pombe*. J. Cell Sci 128, 2259–2268. [PubMed: 25977474]

Aspenström P (2009). Roles of F-BAR/PCH proteins in the regulation of membrane dynamics and actin reorganization. Int. Rev. Cell Mol. Biol 272, 1–31.

Bähler J, Wu J-Q, Longtine MS, Shah NG, McKenzie A, III, Steever AB, Wach A, Philippsen P, and Pringle JR (1998). Heterologous modules for efficient and versatile PCR-based gene targeting in *Schizosaccharomyces pombe*. Yeast 14, 943–951. [PubMed: 9717240]

Begonja AJ, Pluthero FG, Suphamungmee W, Giannini S, Christensen H, Leung R, Lo RW, Nakamura F, Lehman W, Plomann M, et al. (2015). FlnA binding to PACSIN2 F-BAR domain regulates membrane tubulation in megakaryocytes and platelets. Blood 126, 80–88. [PubMed: 25838348]

Carman PJ, and Dominguez R (2018). BAR domain proteins-a linkage between cellular membranes, signaling pathways, and the actin cytoskeleton. Biophys. Rev 10, 1587–1604. [PubMed: 30456600]

Deng L, Kabeche R, Wang N, Wu J-Q, and Moseley JB (2014). Megadalton-node assembly by binding of Skb1 to the membrane anchor Slf1. Mol. Biol. Cell 25, 2660–2668. [PubMed: 25009287]

Frost A, Unger VM, and De Camilli P (2009). The BAR domain superfamily: membrane-molding macromolecules. Cell 137, 191–196. [PubMed: 19379681]

Garabedian MV, Stanishneva-Konovalova T, Lou C, Rands TJ, Pollard LW, Sokolova OS, and Goode BL (2018). Integrated control of forminmediated actin assembly by a stationary inhibitor and a mobile activator. J. Cell Biol 217, 3512–3530. [PubMed: 30076201]

Giloh H, and Sedat JW (1982). Fluorescence microscopy: reduced photobleaching of rhodamine and fluorescein protein conjugates by *n*-propyl gallate. Science 217, 1252–1255. [PubMed: 7112126]

Hansen CG, Howard G, and Nichols BJ (2011). Pacsin 2 is recruited to caveolae and functions in caveolar biogenesis. J. Cell Sci 124, 2777–2785. [PubMed: 21807942]

Itoh T, and Takenawa T (2009). Mechanisms of membrane deformation by lipid-binding domains. Prog. Lipid Res 48, 298–305. [PubMed: 19481110]

Itoh T, Erdmann KS, Roux A, Habermann B, Werner H, and De Camilli P (2005). Dynamin and the actin cytoskeleton cooperatively regulate plasma membrane invagination by BAR and F-BAR proteins. Dev. Cell 9, 791–804. [PubMed: 16326391]

Itoh T, Hasegawa J, Tsujita K, Kanaho Y, and Takenawa T (2009). The tyrosine kinase Fer is a downstream target of the PLD-PA pathway that regulates cell migration. Sci. Signal 2, ra52. [PubMed: 19738202]

Kelley CF, Messelaar EM, Eskin TL, Wang S, Song K, Vishnia K, Becalska AN, Shupliakov O, Hagan MF, Danino D, et al. (2015a). Membrane charge directs the outcome of F-BAR domain lipid binding and autoregulation. Cell Rep. 13, 2597–2609. [PubMed: 26686642]

Kelley LA, Mezulis S, Yates CM, Wass MN, and Sternberg MJ (2015b). The Phyre2 web portal for protein modeling, prediction and analysis. Nat. Protoc 10, 845–858. [PubMed: 25950237]

Laporte D, Coffman VC, Lee I-J, and Wu J-Q (2011). Assembly and architecture of precursor nodes during fission yeast cytokinesis. J. Cell Biol 192, 1005–1021. [PubMed: 21422229]

Lee W-L, Ostap EM, Zot HG, and Pollard TD (1999). Organization and ligand binding properties of the tail of *Acanthamoeba* myosin-IA. Identification of an actin-binding site in the basic (tail homology-1) domain. J. Biol. Chem 274, 35159–35171. [PubMed: 10574999]

Lefèbvre F, Prouzet-Mauléon V, Hugues M, Crouzet M, Vieillemard A, McCusker D, Thoraval D, and Doignon F (2012). Secretory pathway-dependent localization of the *Saccharomyces cerevisiae* Rho GTPase-activating protein Rgd1p at growth sites. Eukaryot. Cell 11, 590–600. [PubMed: 22447923]

Lemmon MA (2004). Pleckstrin homology domains: not just for phosphoinositides. Biochem. Soc. Trans 32, 707–711. [PubMed: 15493994]

Liu S, Xiong X, Zhao X, Yang X, and Wang H (2015). F-BAR family proteins, emerging regulators for cell membrane dynamic changes-from structure to human diseases. J. Hematol. Oncol 8, 47. [PubMed: 25956236]

Liu Y, Lee I-J, Sun M, Lower CA, Runge KW, Ma J, and Wu J-Q (2016). Roles of the novel coiled-coil protein Rng10 in septum formation during fission yeast cytokinesis. Mol. Biol. Cell 27, 2528–2541. [PubMed: 27385337]

Louis-Jeune C, Andrade-Navarro MA, and Perez-Iratxeta C (2012). Prediction of protein secondary structure from circular dichroism using theoretically derived spectra. Proteins 80, 374–381. [PubMed: 22095872]

Martín-García R, Coll PM, and Pérez P (2014). F-BAR domain protein Rga7 collaborates with Cdc15 and Imp2 to ensure proper cytokinesis in fission yeast. J. Cell Sci 127, 4146–4158. [PubMed: 25052092]

McDonald NA, and Gould KL (2016a). Characterization of cytokinetic F-BARs and other membrane-binding proteins. Methods Mol. Biol 1369, 181–189. [PubMed: 26519313]

McDonald NA, and Gould KL (2016b). Linking up at the BAR: oligomerization and F-BAR protein function. Cell Cycle 15, 1977–1985. [PubMed: 27245932]

McDonald NA, Vander Kooi CW, Ohi MD, and Gould KL (2015). Oligomerization but not membrane bending underlies the function of certain F-BAR proteins in cell motility and cytokinesis. Dev. Cell 35, 725–736. [PubMed: 26702831]

Mim C, and Unger VM (2012). Membrane curvature and its generation by BAR proteins. Trends Biochem. Sci 37, 526–533. [PubMed: 23058040]

Moravcevic K, Alvarado D, Schmitz KR, Kenniston JA, Mendrola JM, Ferguson KM, and Lemmon MA (2015). Comparison of *Saccharomyces cerevisiae* F-BAR domain structures reveals a conserved inositol phosphate binding site. Structure 23, 352–363. [PubMed: 25620000]

Pollard TD (2010). A guide to simple and informative binding assays. Mol. Biol. Cell 21, 4061–4067. [PubMed: 21115850]

Pylypenko O, Lundmark R, Rasmuson E, Carlsson SR, and Rak A (2007). The PX-BAR membrane-remodeling unit of sorting nexin 9. EMBO J 26, 4788–4800. [PubMed: 17948057]

Qualmann B, Koch D, and Kessels MM (2011). Let's go bananas: revisiting the endocytic BAR code. EMBO J 30, 3501–3515. [PubMed: 21878992]

Roberts-Galbraith RH, and Gould KL (2010). Setting the F-BAR: functions and regulation of the F-BAR protein family. Cell Cycle 9, 4091–4097. [PubMed: 20948299]

Rothbauer U, Zolghadr K, Muyldermans S, Schepers A, Cardoso MC, and Leonhardt H (2008). A versatile nanotrap for biochemical and functional studies with fluorescent fusion proteins. Mol. Cell. Proteomics 7, 282–289. [PubMed: 17951627]

Salzer U, Kostan J, and Djinović-Carugo K (2017). Deciphering the BA R code of membrane modulators. Cell. Mol. Life Sci 74, 2413–2438. [PubMed: 28243699]

Schuck P (2000). Size-distribution analysis of macromolecules by sedimentation velocity ultracentrifugation and lamm equation modeling. Biophys. J 78, 1606–1619. [PubMed: 10692345]

Senju Y, Itoh Y, Takano K, Hamada S, and Suetsugu S (2011). Essential role of PACSIN2/syndapin-II in caveolae membrane sculpting. J. Cell Sci 124, 2032–2040. [PubMed: 21610094]

Shimada A, Niwa H, Tsujita K, Suetsugu S, Nitta K, Hanawa-Suetsugu K, Akasaka R, Nishino Y, Toyama M, Chen L, et al. (2007). Curved EFC/F-BAR-domain dimers are joined end to end into a filament for membrane invagination in endocytosis. Cell 129, 761–772. [PubMed: 17512409]

Shoham NG, Centola M, Mansfield E, Hull KM, Wood G, Wise CA, and Kastner DL (2003). Pyrin binds the PSTPIP1/CD2BP1 protein, defining familial Mediterranean fever and PAPA syndrome as disorders in the same pathway. Proc. Natl. Acad. Sci. USA 100, 13501–13506. [PubMed: 14595024]

Soulard A, Lechler T, Spiridonov V, Shevchenko A, Shevchenko A, Li R, and Winsor B (2002). *Saccharomyces cerevisiae* Bzz1p is implicated with type I myosins in actin patch polarization and is able to recruit actin-polymerizing machinery *in vitro*. Mol. Cell. Biol 22, 7889–7906. [PubMed: 12391157]

Takeda T, Robinson IM, Savoian MM, Griffiths JR, Whetton AD, McMahon HT, and Glover DM (2013). Drosophila F-BAR protein Syndapin contributes to coupling the plasma membrane and contractile ring in cytokinesis. Open Biol 3, 130081. [PubMed: 23926047]

Taylor MJ, Perrais D, and Merrifield CJ (2011). A high precision survey of the molecular dynamics of mammalian clathrin-mediated endocytosis. PLoS Biol 9, e1000604. [PubMed: 21445324]

Willet AH, McDonald NA, Bohnert KA, Baird MA, Allen JR, Davidson MW, and Gould KL (2015). The F-BAR Cdc15 promotes contractile ring formation through the direct recruitment of the formin Cdc12. J. Cell Biol 208, 391–399. [PubMed: 25688133]

Woods A, Sherwin T, Sasse R, MacRae TH, Baines AJ, and Gull K (1989). Definition of individual components within the cytoskeleton of *Trypanosoma brucei* by a library of monoclonal antibodies. J. Cell Sci 93, 491–500. [PubMed: 2606940]

Wu J-Q, and Pollard TD (2005). Counting cytokinesis proteins globally and locally in fission yeast. Science 310, 310–314. [PubMed: 16224022]

Yamamoto H, Itoh N, Kawano S, Yatsukawa Y, Momose T, Makio T, Matsunaga M, Yokota M, Esaki M, Shodai T, et al. (2011). Dual role of the receptor Tom20 in specificity and efficiency of protein import into mitochondria. Proc. Natl. Acad. Sci. USA 108, 91–96. [PubMed: 21173275]

Zhu Y-H, Ye Y, Wu Z, and Wu J-Q (2013). Cooperation between Rho-GEF Gef2 and its binding partner Nod1 in the regulation of fission yeast cytokinesis. Mol. Biol. Cell 24, 3187–3204. [PubMed: 23966468]

Highlights

- The Rga7 F-BAR domain binds Rng10 and the plasma membrane simultaneously
- The Rga7-Rng10 interaction significantly enhances Rga7 membrane avidity
- Rga7 F-BAR function can be bypassed by tethering the remainder of Rga7 to Rng10
- Some F-BAR domains are necessary but not sufficient for plasma membrane targeting

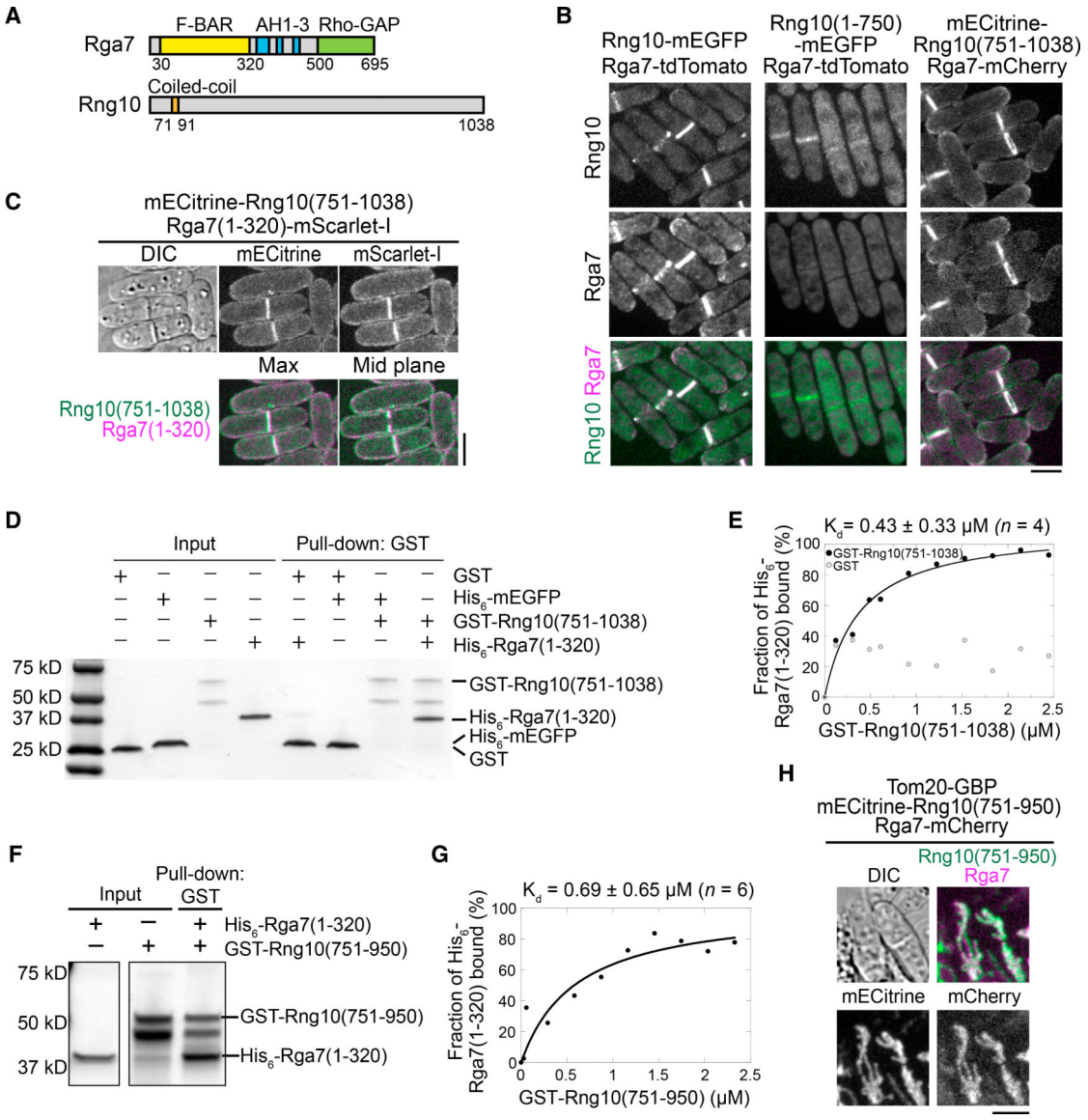

Figure 1. The C Terminus of Rng10 Is Required for Rga7 Localization through Direct Interaction with the Rga7 F-BAR Domain

(A) Domain schematics of Rga7 and Rng10. Amphipathic helices (AH1–3) overlap with a proline-rich region in Rga7 (Arasada and Pollard, 2015; Martín-García et al., 2014).

(B) Colocalization images showing that Rga7 localization requires the Rng10 C terminus. All tagged yeast genes or truncations in this study are at their native chromosomal loci and under endogenous promoters, except where noted. See also Figures S1A–S1C.

(C) Colocalization of Rng10(751–1,038) and Rga7(1–320).

(D) *In vitro* binding of GST-Rng10(751–1,038) and His_6-Rga7(1–320). Bead bound GST-Rng10(751–1,038) or a GST control was incubated with His_6-Rga7(1–320) or an His_6-mEGFP control.

(E) Measurement of affinity (K_d) between Rng10(751–1,038) and Rga7(1–320) by supernatant depletion assay.

(F) *In vitro* binding of GST-Rng10(751–950) and His_6-Rga7(1–320).

(G) Measurement of affinity between Rng10(751–950) and Rga7(1–320). See also Figures S2A and S2B.

(H) Micrographs showing that Rng10(751–950) mislocalizes Rga7 to mitochondria by Tom20-GBP. See also Figures S1D and S1E. Scale bars, 5 μm.

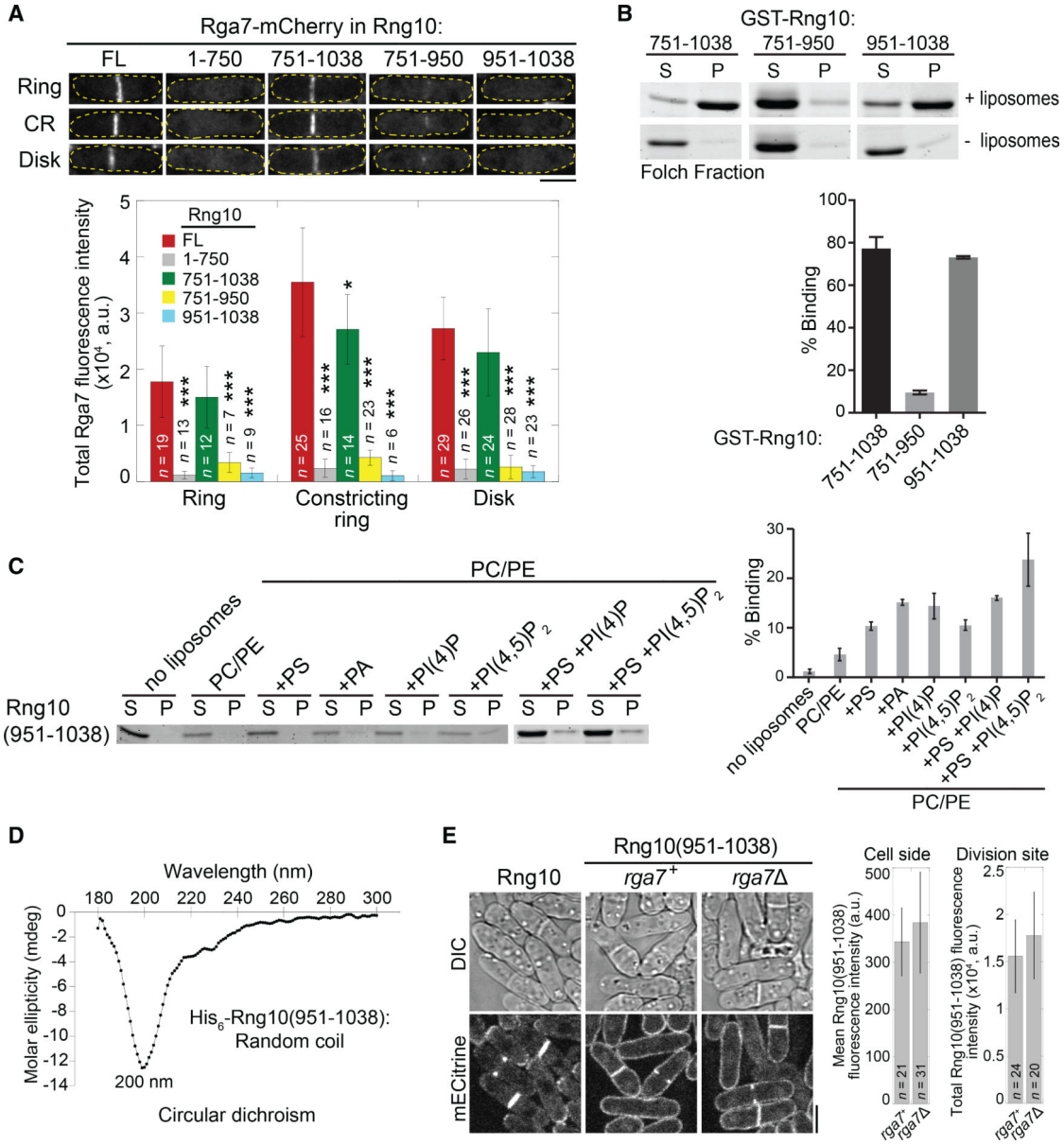

Figure 2. The Unstructured C-Terminal Tail of Rng10 Binds Membranes and Is Crucial for Rga7 Localization

(A) Rga7 localization (top) and protein levels (bottom) at the division site in *rng10* mutants. Cells are grouped into three stages: ring (compact ring before constriction), constricting ring (CR, Rga7 occupies part of the division plane during ring constriction), and disk (Rga7 spreads to the whole division plane). Data are mean ± 1 SD. *p < 0.01 and ***p < 0.0001 compared to FL Rng10. See also Figure S2E.

(B) Top: liposome-binding assay showing that Rng10(951–1,038) binds liposomes *in vitro*. S, supernatant (unbound); P, pellet (bound) fractions. Bottom: quantification of bound Rng10 (n = 3).

(C) Left: Rng10(951–1,038) binding to liposomes of various lipid compositions. Liposomes contained 15% phosphatidylethanolamine (PE), 10% phosphatidylserine (PS) when

indicated, 5% of various PIPs when indicated, and the remainder was phosphatidylcholine (PC). Right: quantification of bound Rng10 (n = 3).

(D) Far-UV circular dichroism of His_6-Rng10(951–1,038).

(E) Left: localization of FL Rng10 and Rng10(951–1,038) in *rga7*$^+$ and *rga7*Δ cells in the middle focal plane. Quantifications (right) of Rng10(951–1,038) membrane levels at cell sides (middle slice of interphase cells) and the division site (sum intensity of cells with closed septa). Mean ± 1 SD. Scale bars, 5 μm.

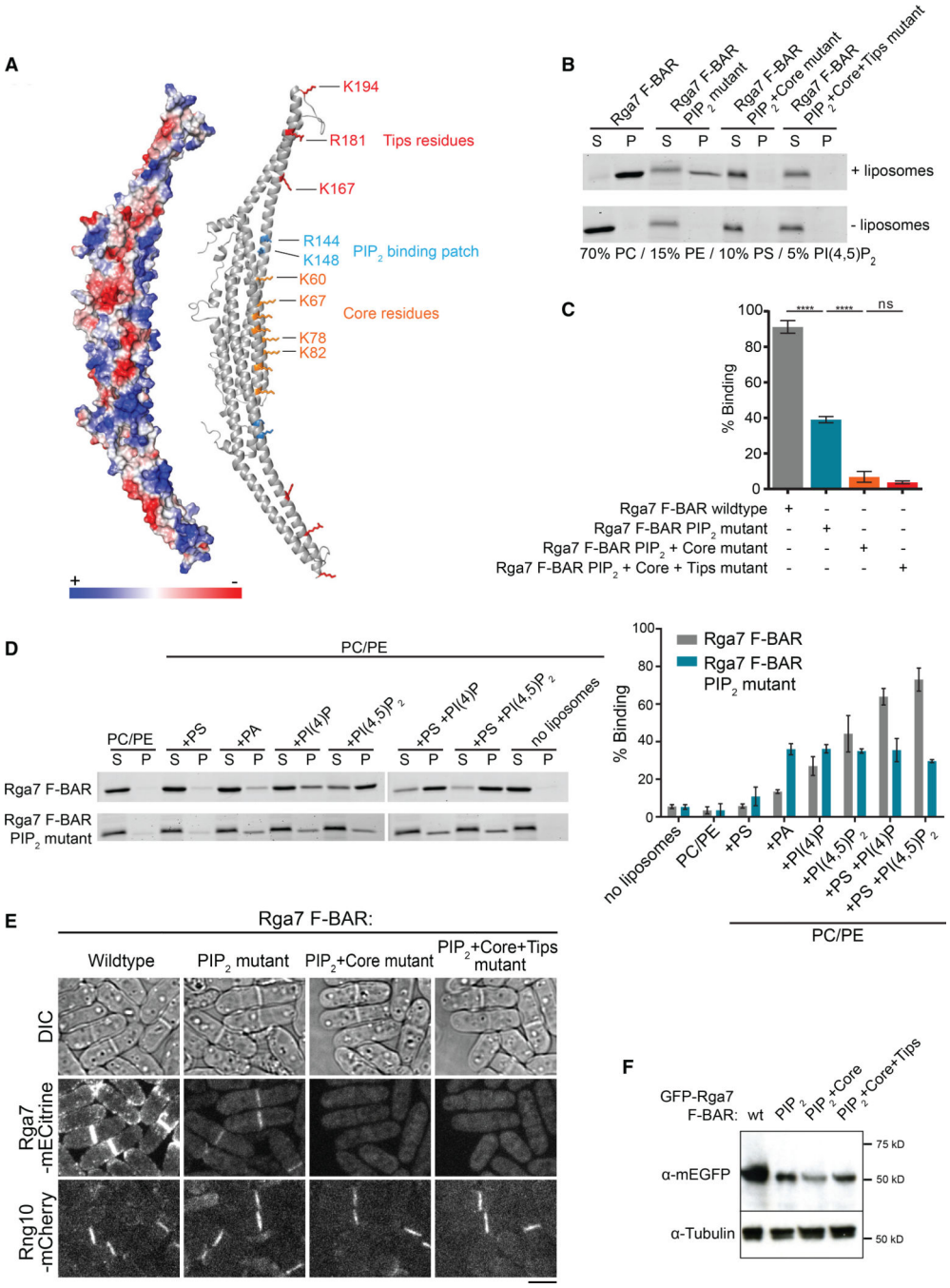

Figure 3. Mechanism of Rga7 F-BAR Membrane Binding

(A) Structural model of the Rga7 F-BAR dimer based on homologous Rgd1 (PDB:4WPE) with putative membrane interaction residues highlighted.

(B) The indicated patches of residues in (A) were mutated to residues as described in the Method Details and tested for liposome binding. S, supernatant (unbound); P, pellet (bound) fractions.

(C) Quantification of bound Rga7 from (B) (n = 3). ****$p < 0.0001$. See also Figures S2F, S2G, and S3A–S3C.

(D) Rga7 F-BAR prefers membranes rich in PIPs, especially $PI(4,5)P_2$. Liposomes contained 15% PE, 10% PS when indicated, 5% of various PIPs when indicated, and the remainder was PC.

(E) Localization of Rga7 F-BAR mutants in cells with FL Rng10. Scale bar, 5 μm. See also Figure S3D.

(F) Western blot examining Rga7 F-BAR constructs levels. Tubulin serves as a loading control.

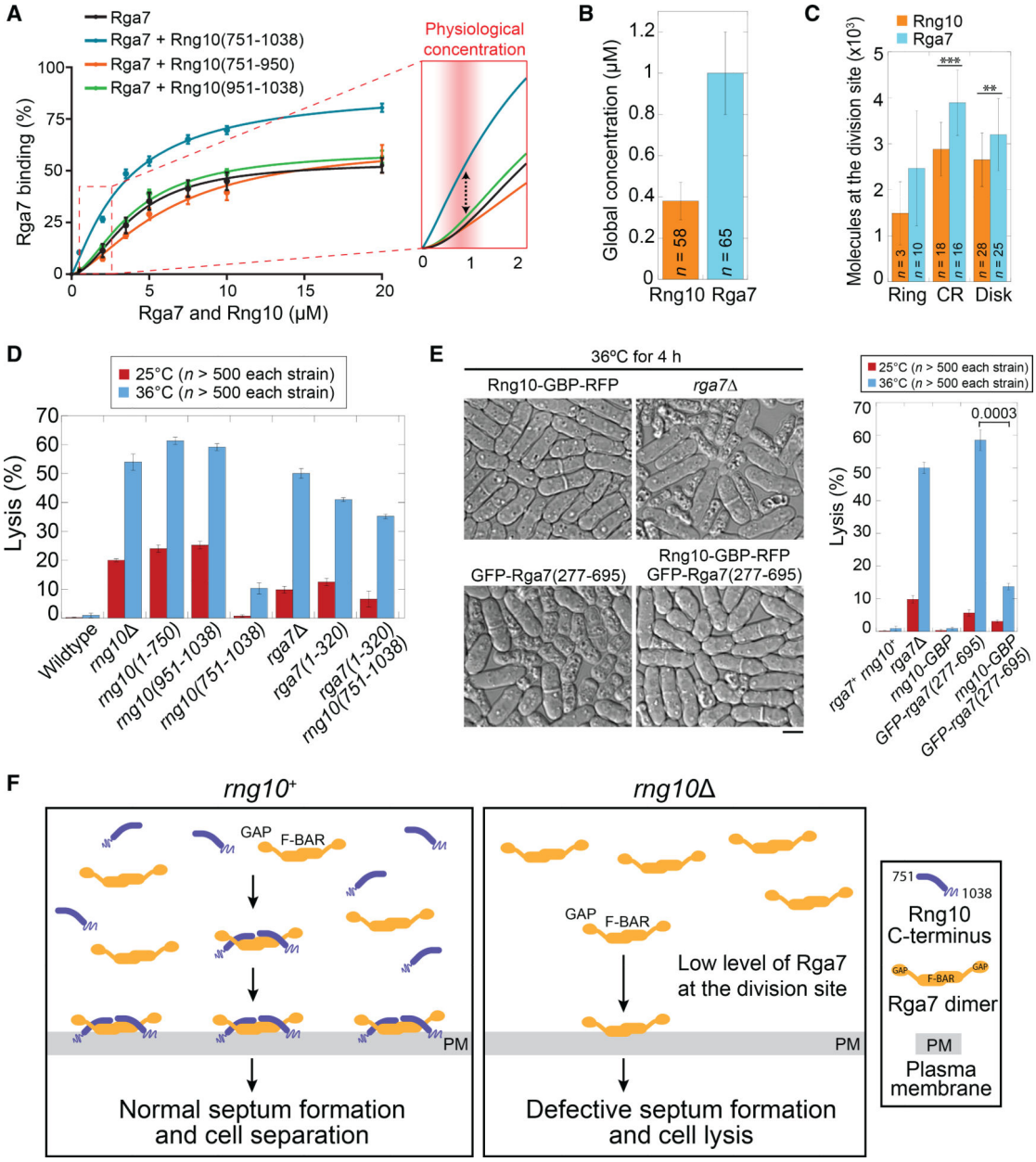

Figure 4. The Rng10-Rga7 Complex Enhances Rga7 Membrane Binding at Physiological Concentrations to Support Septation

(A) *In vitro* liposome binding assays of equimolar Rga7 and Rng10 with liposomes containing 70% PC/15% PE/10% PS/5% PI(4,5)P_2. The red inset shows the increase in the binding of the Rng10-Rga7 complex at the physiological concentration range determined in (B).

(B) Global concentrations of Rng10 and Rga7.

(C) Rng10 and Rga7 molecules at the division site. **p < 0.001 and ***p < 0.0001.

(D) Quantification of cell lysis in rga7 and *rng10* mutants.

(E) Differential interference contrast (DIC) images (left) and quantifications (right) showing that Rng10-GBP rescues the lysis phenotype of GFP-Rga7(277–695). p value listed on top. Scale bar, 5 μm. Mean ± 1 SD in (B)–(E). See also Figure S3E.

(F) A model for Rng10 enhancing Rga7 division-site targeting. The Rng10 C terminus simultaneously interacts with the Rga7 F-BAR domain and the PM to increase the membrane affinity of Rga7.

KEY RESOURCE TABLE

REAGENT or RESOURCE	SOURCE	IDENTIFIER
Antibodies		
Anti-GFP	Roche	11814460001; RRID: AB_390913
TAT1	Keith Gull (Woods et al., 1989)	N/A
Anti-mouse immunoglobulin G	Sigma-Aldrich	A4416; RRID: AB_258167
Monoclonal anti-His	Clontech	631212; RRID: AB_2721905
Anti-GST	Novus Biologicals	NB600–446; RRID: AB_10003107
Anti-mouse fluorescent antibody	LI-COR	92568070; RRID: AB_2651128
Bacterial and Virus Strains		
BL21(DE3)pLysS	Novagen	694513
Chemicals, Peptides, and Recombinant Proteins		
Gelatin	Sigma-Aldrich	G2500
Protease inhibitor	Roche	11873580001
Lipid chloroform stocks	Avanti Polar Lipids	N/A
CellMask Deep Red	Thermo Fisher Scientific	C10046
SuperSignal West Maximum Sensitivity Substrate	Thermo Fisher Scientific	34096
Glutathione-Sepharose beads	GE Healthcare	17-5132-01
Talon metal affinity resin	Clontech	635501
Experimental Models: Organisms/Strains		
See Table S1	This study	N/A
Software and Algorithms		
ImageJ	NIH	https://imagej.nih.gov/ij/
Other		
Liposome extruder	Avanti Polar Lipids	610023
BioMax MR film	Kodak	Z350370
Epifluorescence microscope	Nikon	Eclipse Ti
UltraVIEW spinning disk confocal system	PerkinElmer	Vox CSUX1
Personal Deltavision system	GE Healthcare	N/A